Structural and functional investigation of graphene oxide–Fe3O4 nanocomposites for the heterogeneous Fenton-like reaction

Nor Aida Zubir, Christelle Yacou, Julius Motuzas, Xiwang Zhang, João C. Diniz da Costa

SCIENTIFIC REPORTS

OPEN

SUBJECT AREAS:
CHEMICAL ENGINEERING
NANOPARTICLES

Received
14 January 2014

Accepted
19 March 2014

Published
4 April 2014

Correspondence and requests for materials should be addressed to J.C.D.d.C. (j.dacosta@uq.edu.au)

Structural and functional investigation of graphene oxide–Fe_3O_4 nanocomposites for the heterogeneous Fenton-like reaction

Nor Aida Zubir[1,2], Christelle Yacou[1], Julius Motuzas[1], Xiwang Zhang[3] & João C. Diniz da Costa[1]

[1]The University of Queensland, FIMLab—Films and Inorganic Membrane Laboratory, School of Chemical Engineering, Brisbane, Qld 4072, Australia, [2]Universiti Teknologi MARA (UiTM), Faculty of Chemical Engineering, 13500 Pulau Pinang, Malaysia, [3]Department of Chemical Engineering, Monash University, Clayton, VIC 3800, Australia.

Graphene oxide–iron oxide (GO–Fe_3O_4) nanocomposites were synthesised by co-precipitating iron salts onto GO sheets in basic solution. The results showed that formation of two distinct structures was dependent upon the GO loading. The first structure corresponds to a low GO loading up to 10 wt%, associated with the beneficial intercalation of GO within Fe_3O_4 nanoparticles and resulting in higher surface area up to 409 $m^2 g^{-1}$. High GO loading beyond 10 wt% led to the aggregation of Fe_3O_4 nanoparticles and the undesirable stacking of GO sheets. The presence of strong interfacial interactions (Fe-O-C bonds) between both components at low GO loading lead to 20% higher degradation of Acid Orange 7 than the Fe_3O_4 nanoparticles in heterogeneous Fenton-like reaction. This behaviour was attributed to synergistic structural and functional effect of the combined GO and Fe_3O_4 nanoparticles.

Magnetite (Fe_3O_4) has attracted considerable research interests in materials chemistry because of its unique properties, including decent magnetic, electric, catalytic, biocompatibility and low toxicity properties[1–4]. In particular, Fe_3O_4 nanoparticles (NPs) have been reported to be a catalyst in many reactions such as Fischer-Tropsch[5], Haber-Bosch[6,7], environmental catalysis[3,8,9], and peroxidase-like activities[10–12]. However, these NPs are prone to aggregate and form large particles owing to strong anisotropic dipolar interactions specifically in aqueous phase, thus losing their dispersibility and specific properties which eventually diminish their activity[13]. Therefore, there is a need to immobilise these NPs onto supports to preserve their unique properties[14–16].

Among many materials, graphene and its derivatives are considered potential materials for the immobilisation of NPs. Of particular interest, graphene oxide (GO) is an attractive material due to its unique two-dimensional lamellar structure and high surface area as well as full surface accessibility and edge reactivity[1,17]. The immobilised NPs are not only able to prevent the aggregation of graphene or GO from stacking but also improve the overall catalytic activity owing to the strong synergistic interaction between both components[18,19]. The lack of surface functionalities in graphene to directly immobilise the NPs onto its surfaces has led to favourable utilisation of GO as an alternative support for the assembly of graphene based nanocomposites[20].

GO is derived from the exfoliation of graphite oxide and consists of abundant oxygenated functional groups, such as hydroxyl and epoxides on the basal plane with carbonyl and carboxyl groups at the edges. These oxygenated functional groups can serve as nucleation sites for metal ions to form NPs/GO nanocomposites. Recently, several studies have been reported using GO for the support of Fe_3O_4 NPs in catalysis for the reduction of nitrobenzene[21], the oxidation of cysteine[22] and 3,3,5,5-tetramethylbenzidine[23]. The reported enhancement in catalytic activity was attributed to the synergistic effects between both GO sheets and Fe_3O_4 NPs.

This work primarily focuses on developing nanocomposite structures containing graphene oxide and iron oxide (GO–Fe_3O_4). The resultant GO–Fe_3O_4 nanocomposites were synthesised via depositing Fe_3O_4 NPs on GO sheets by co-precipitation method. The nanocomposites were then extensively characterised using nitrogen sorption, transmission electron microscopy (TEM) and X-ray photoelectron spectroscopy (XPS), to better understand their structures and functionalities. Finally, the catalytic activity of the nanocomposites in the degradation of Acid Orange 7 (AO7) dye was evaluated in a heterogeneous Fenton-like reaction. The results provide a new insight into

the development of GO–Fe_3O_4 nanocomposites and the structural-morphology relationships with their catalytic activity.

Results

The nitrogen sorption measurements were performed to investigate the textural characteristics of resultant nanocomposites at different GO loading, varying from 0 to 25 wt%. The nitrogen isotherms in Fig. 1a resulted in type IV shape with H2 hysteresis loop in the range of 0.3–0.98 relative pressure. These results suggest that the GO–Fe_3O_4 nanocomposites are characterised by mesoporous structures. The pore size distribution curves (Fig. 1b) calculated using DFT model display pore sizes in the range from 1 to 10 nm. In contrast to the GO–Fe_3O_4 nanocomposites, Fe_3O_4 NPs show a much broader pore size distribution up to 20 nm. Such vicissitudes in hysteresis and pore size distribution may be ascribed to the role played by GO in tailoring the pore structure of the nanocomposites. This stems from integrating two-dimensional (GO sheets) and zero-dimensional (Fe_3O_4 NPs) structures into a single material[24].

The specific surface area and pore volumes of the prepared Fe_3O_4 NPs and nanocomposites are presented in Fig. 1c. A noteworthy increment in surface area was observed by increasing GO loading from 5 to 10 wt% (max S_{BET} approximately 409 $m^2\ g^{-1}$), which declined thereafter. Indeed, a similar observation was also found in pore volume. At low GO loading (≤10 wt%), the pore volume remained steady at ~0.32–0.33 $cm^3\ g^{-1}$ and subsequently decreased to ~0.23–0.24 $cm^3\ g^{-1}$ at higher GO loading (>10 wt%).

Figs. 2a–b show the micrographs of pure GO sheets where the surface dimensions are of several microns and thickness of ~30 nm. Fe_3O_4 NPs are agglomerated (Figs. 2c–d), evidenced by formation of large clusters. Figs. 2e–f and 2g–h show the micrographs of the 5 and 15 wt% GO nanocomposites, respectively. Compared to the pristine GO sheets (Fig. 2a–b), it can be distinctly seen that Fe_3O_4 NPs were deposited onto GO surfaces of the nanocomposites. Moreover, no isolated Fe_3O_4 NPs were observed beyond the GO, suggesting a strong interaction between the NPs and GO sheets. It is also observed a significant reduction in the thickness of the layers for the 5 wt% GO loading, calculated from 2 to 3 nm around Fe_3O_4 NPs, or up to ~5 nm as a combination of these layers (see broken line box at the inset of Fig. 2f). For the 15 wt% GO loading, the Fe_3O_4 NPs agglomerated on the external GO surface, and GO layer thickness could not be measured.

Although a minor degree of aggregation occurs at low GO loading (5 wt%), most of the Fe_3O_4 NPs are still highly dispersed on the GO sheets (Fig. 2e). It is further observed the NPs were intercalated between the GO sheets (see the inset broken line box in Fig. 2f). This observation suggests that the low GO loading helped to prevent Fe_3O_4 from severe aggregation, which is beneficial for the distribution of NPs over the GO planes. The bright circular rings in the selected area electron diffraction (SAED) patterns indicate that Fe_3O_4 NPs are polycrystalline. The spaced-resolved lattice fringes with an interplanar distance of 0.25 nm agree well with the lattice spacing of (311) planes of Fe_3O_4 as reported elsewhere[20,25].

However, a higher GO loading (15 wt%) shows the formation of a different structure. This is clearly seen in the HRTEM micrograph (Fig. 2h) where the surface no longer displays the GO sheets as in Figs. 2a and 2e–f. In fact, Fig. 2h exhibits patterns similar to the pure Fe_3O_4 NPs in Fig. 2d. These images are evidencing that a higher

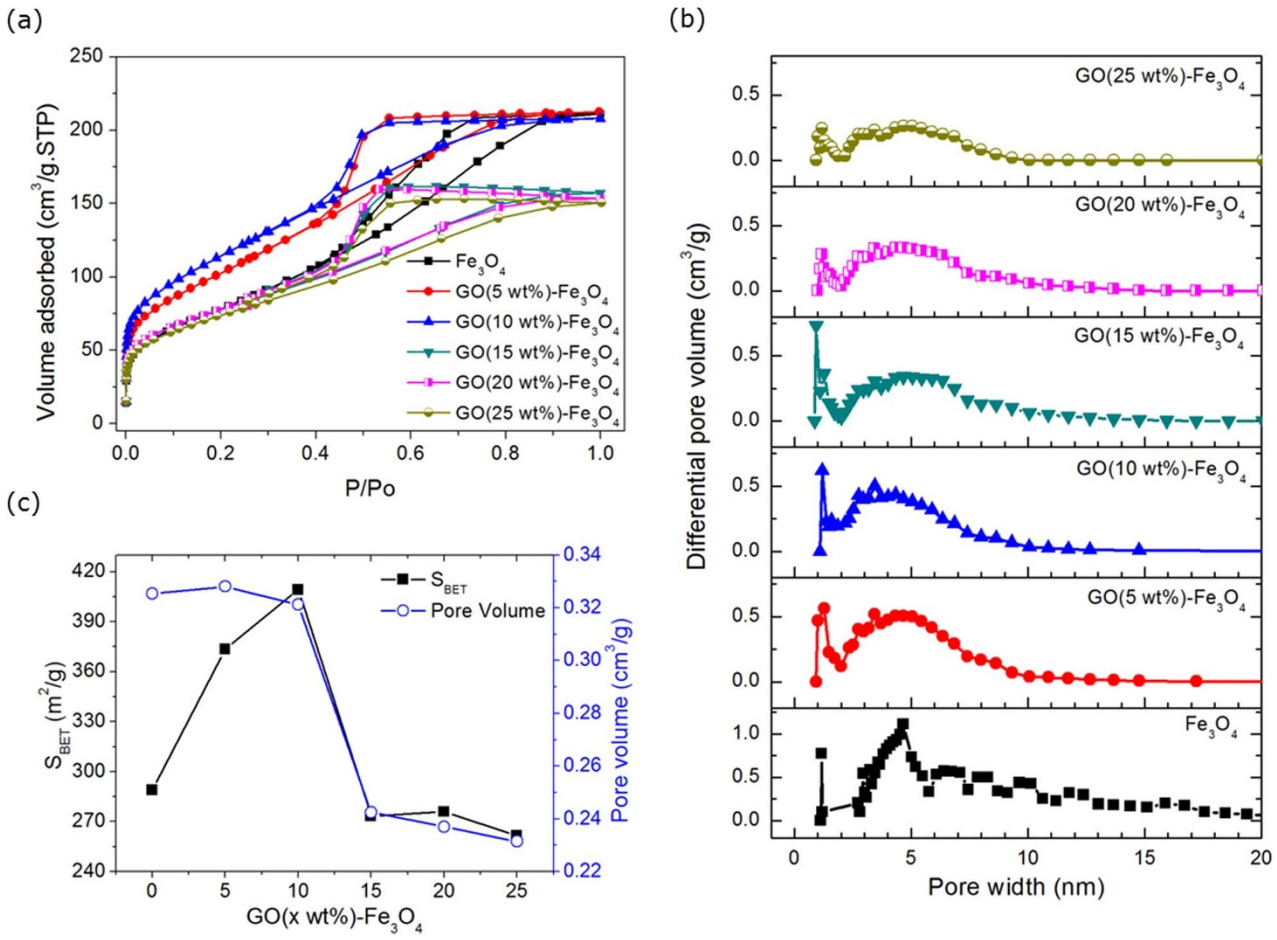

Figure 1 | (a) Nitrogen adsorption-desorption isotherms, (b) DFT pore size distributions and (c) S_{BET} and pore volume of Fe_3O_4 and GO–Fe_3O_4 nanocomposites at various GO loadings.

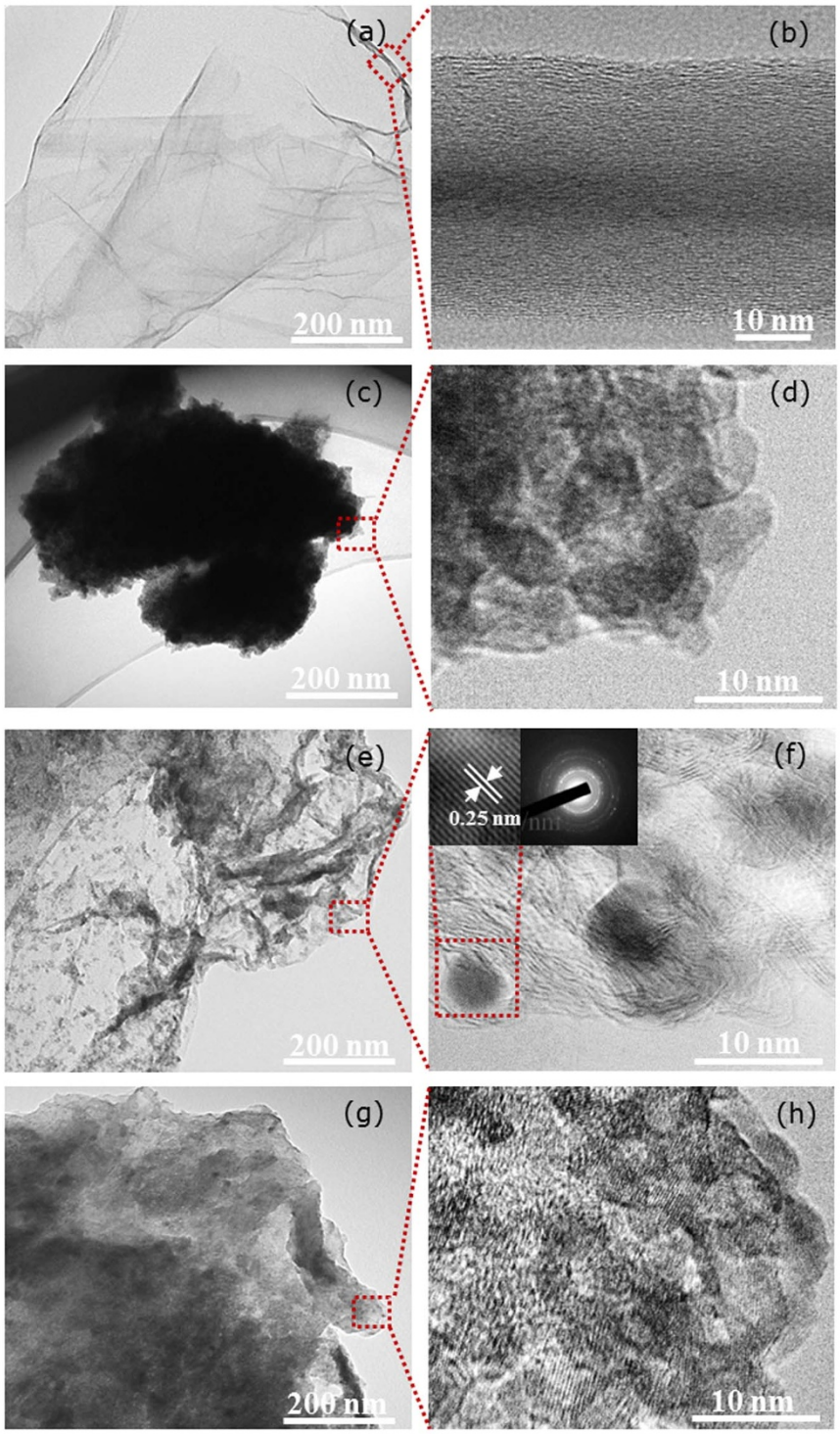

Figure 2 | TEM images of (a–b) GO, (c–d) Fe_3O_4 NPs, (e–f) GO(5 wt%)–Fe_3O_4 nanocomposite and (g–h) GO(15 wt%)–Fe_3O_4 nanocomposite.

degree of aggregation of Fe_3O_4 NPs prevails once the GO loading reached 15 wt%, which is coherent with the reduction in pore volume (Fig. 1c). The dominant coverage of Fe_3O_4 NPs is attributed to the oxygenated functional groups on the exterior surface of GO stacking, which tend to facilitate the nucleation and growth of the NPs. This process is similar to many cases where the surface defects and edges provide thermodynamically favourable nucleation sites[26], which show heavy agglomeration as seen in Figs. 2c–d.

The prepared nanocomposites were then further analysed using XPS to verify the phase of NPs, interaction between NPs and GO and state of GO as supports. As seen in Fig. 3a, the wide scan spectra of the nanocomposites exhibited photoelectron lines at binding energies of ~285, 530 and 711 eV which are ascribed to C 1s, O 1s and Fe 2p, respectively. The binding energy peaks at 711.1 and 724.6 eV in the high resolution Fe 2p scan (Fig. 3b) correspond to Fe $2p_{3/2}$ and Fe $2p_{1/2}$, respectively. The disappearance of the charge transfer satellite of Fe $2p_{3/2}$ at ~720 eV reveals the formation of mixed oxide of Fe(II) and Fe(III) namely as Fe_3O_4[1,27]. Besides, similar peak patterns were attained with different GO loadings, indicating the formation of Fe_3O_4 phase in all nanocomposites.

Fig. 4a shows the O 1s spectra of GO, GO–Fe_3O_4 nanocomposites and Fe_3O_4 NPs. The deconvolution of the O 1s spectrum of GO

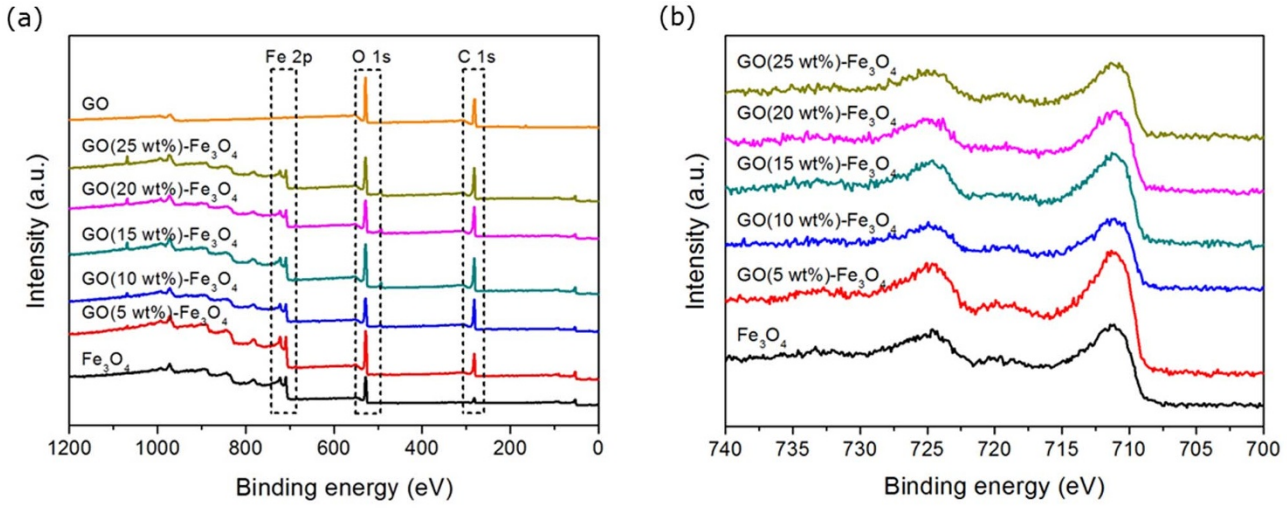

Figure 3 | (a) Wide scan XPS spectra and (b) high resolution Fe 2p spectra of GO, GO–Fe_3O_4 nanocomposites and Fe_3O_4 NPs.

consists of three peaks: (i) the oxygen that binds to the sulphate group owing to slight trace of sulphur detected at 168 eV in wide scan spectra (O ex SO_4: 531.4 eV), (ii) the oxygen in carboxylate and/or carbonyl (O–C = O; C = O: 532.4 eV), and (iii) the oxygen in the epoxy and/or hydroxyl (C–O–C; C–OH: 533.2 eV). It is notable that the peaks of O 1s in GO–Fe_3O_4 nanocomposites spectra shifted to lower binding energy and broadened, which is characteristic of the O 1s belonging to lattice oxygen in Fe_3O_4 (Fe–O: 529.8 eV)[26].

The binding of Fe_3O_4 on GO might possibly occur through either the carbon atoms or with the oxygenated functional groups on both GO surfaces and edges. However, the first possibility is excluded as the contribution from C or Fe atoms in the Fe–C bonds are not present at 707.5[28] and 283.3 eV[29] in both Fe 2p (Fig. 3b) and C 1s (Fig. 4b) spectra of the nanocomposites, respectively. Therefore, we postulate that the emergence of the new peak at about 531.2 eV in the nanocomposites spectra is assigned to the deposition of Fe_3O_4 NP onto GO sheets, which is possibly via Fe–O–C bonds. Such postulation can be supported by the significant decrease in the relative intensity of O–C = O, C = O and C–O–C, and C–OH peaks in the nanocomposites compared to the pristine GO, which suggests possible bidentate coordination of the Fe element with carboxylate groups[23,30] and replacement of hydrogen in hydroxyl groups. Further considerations could be related to a ring opening reaction of epoxy groups[31,32] by Fe element in Fe_3O_4 through the Fe–O–C bonds. The O 1s spectrum of Fe_3O_4 NPs displays a maximum peak centred at 529.8 eV which is ascribed to the Fe–O bonds. This finding can be substantiated by the fact that the formation of metal–O–C bonds in nanocomposites could be shifted to higher binding energy approximately 1–3 eV from the metal–O bonds of metal oxides[28,32–34] as presented in Table 1.

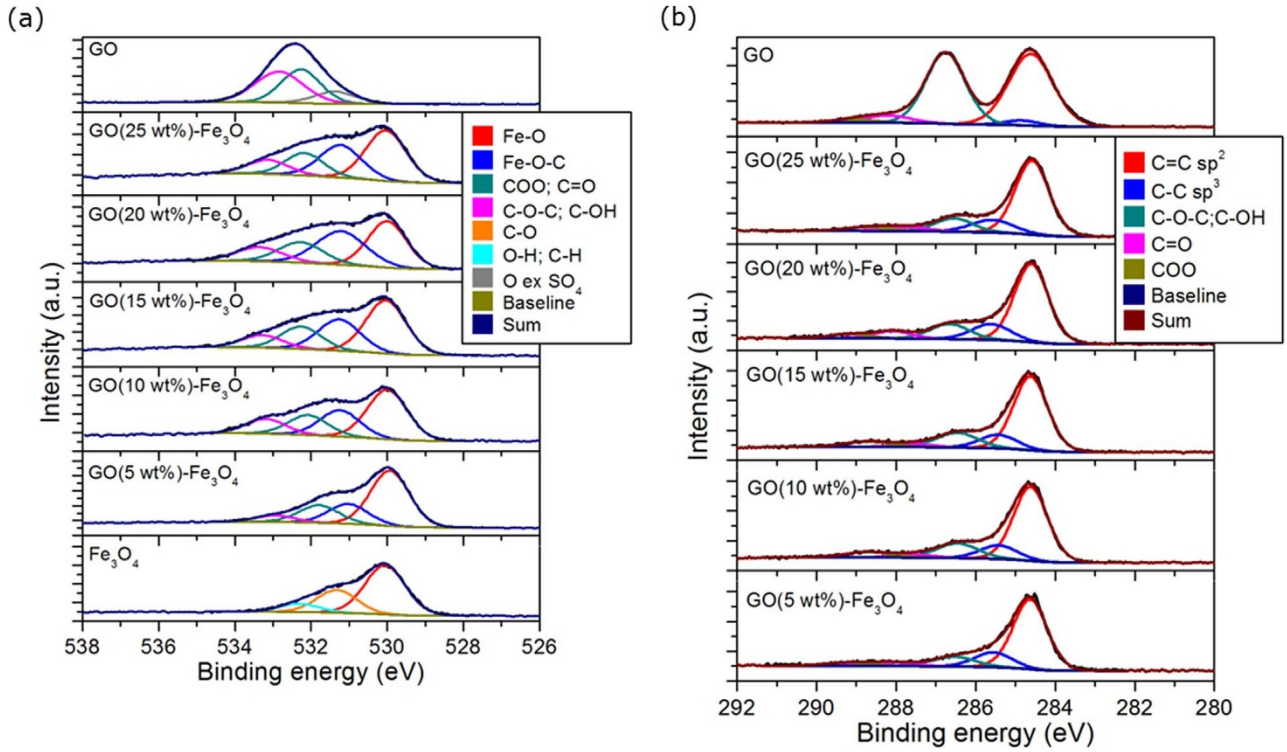

Figure 4 | XPS curve fit of (a) O 1s and (b) C 1s spectra.

Table 1 | Binding energy (B.E.) of metal–O–C bonds in O 1s spectra

Metal–O bond	B.E. (eV)	Metal–O–C bond	B.E. (eV)	Refs.
Fe–O	530.3	Fe–O–C	531.7	28
		Fe–O–C	533.0	33
Fe–O	529.8	Fe–O–C	531.2	This work
Ni–O	529.3	Ni–O–C	530.2	32
Cu–O	530.5	Cu–O–C	532.8	34

The state of GO as a support in these nanocomposites is further demonstrated by the C 1s spectra as shown in Fig. 4b. The spectrum of GO can be deconvoluted into five components corresponding to C = C sp^2 (284.6 eV), C–C sp^3 (285.1 eV), C–OH and/or C–O–C (286.7 eV), C = O (288.1 eV) and O–C = O (289.0 eV)[17,35,36]. It is observed that the intensity of C–OH and C–O–C peak is alike with the C = C sp^2, suggesting that GO is adequately oxidised and holds lots of hydroxyl and epoxy groups as compared to the carbonyl and carboxylate groups. Interestingly, the peak of C–C sp^3 in GO–Fe_3O_4 nanocomposites shifted to higher binding energy by 0.4 eV. This peak increased in its intensity together with C = C sp^2 upon the deposition of Fe_3O_4, while the oxygenated functional groups decreased, particularly for C–OH and C–O–C as the GO loading reduces. These results suggest the likelihood of GO to undergo partial reduction due to partial removal of epoxide and hydroxyl group on GO basal plane, which were deoxygenated under alkaline conditions during the preparation of GO–Fe_3O_4 nanocomposites.

Additionally, the formation of a new covalent bond, Fe–O–C, and the partial reduction in GO as supports for these nanocomposites were reaffirmed based on the atomic concentration and its respective ratio of deconvoluted peaks from O 1 s and C 1 s spectra (Fig. 4). The summarised data deduced from the respective peaks are presented in Fig. 5. The emergence of Fe–O–C bond was found to increase gradually in low GO loading (<10 wt%) and tends to level off once reaching 10 wt%. As the GO loading increases, the amount of Fe_3O_4 deposited raises progressively with the readily available oxygenated functional groups within the exfoliated GO sheets by the successful intercalation between both components. However, further increasing the GO loading (beyond 10 wt%) leads to the saturation of Fe–O–C bonding close to 25%, that possibly infers to a change in structure. The C = O/Fe–O ratio from the O 1 s spectra were found to increase gradually as a function of the GO loading, which signifies

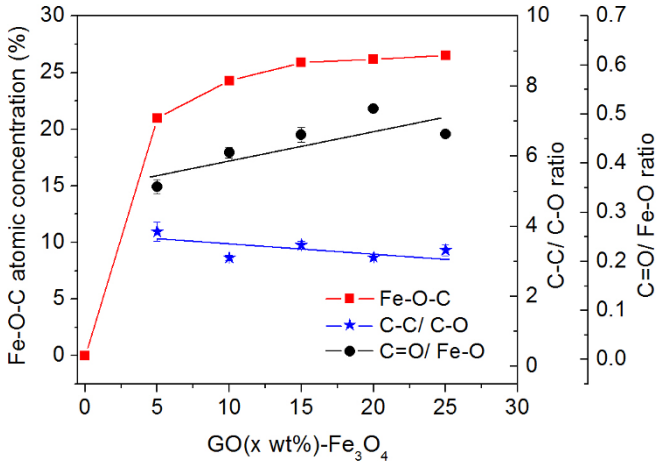

Figure 5 | Correlations between the Fe–O–C atomic content, C–C/C–O and C = O/Fe–O atomic ratio with increased in GO loading of GO–Fe_3O_4 nanocomposites.

higher GO's reduction can be obtained at lower loading compared to the higher one. Intriguingly, this finding can be verified by the ratio of atomic concentration for the carbon domain over the oxygenated functional groups (C–C/C–O) of GO in the C 1 s spectra of nanocomposites. The ratio of C–C/C–O declines steadily from 4 to nearly 3 with increasing GO loading, compared to the pristine GO value of 1. This correlation further corroborate with the state of GO as a support which undergoes partial reduction during co-precipitation through the gradual removal of oxygenated functional groups from its surfaces and edges.

The catalysis of GO–Fe_3O_4 nanocomposites and each individual component for the degradation of AO7 as the model organic pollutant was investigated in the heterogeneous Fenton-like reaction as shown in Fig. 6. The low GO loading (≤10 wt%) nanocomposites led to higher AO7 degradation within 92–98% of removal compared with lower values for pristine Fe_3O_4 NPs and GO. However, the removal efficiency of AO7 at higher GO loading (>10 wt%) declined gradually from 88 to 60% possibly attributed to the structural makeup of the nanocomposite.

Discussion

As the operation of heterogeneous Fenton-like reaction involved in concurrent adsorption and reactions at the solid-liquid interface, the surface accessibility of the GO–Fe_3O_4 nanocomposites is crucial in maintaining their catalytic activity. High accessibility of reactants towards the active sites ($\equiv Fe^{2+}/\equiv Fe^{3+}$) at low GO loading can be achieved by the increase of surface area and pore volume (Fig. 1c), which are able to diminish limitations in mass transfer during the reaction. This can be correlated with their unique structures as schematically represented in Fig. 7. The proposed structures are relying on the degree of GO loading, wherein the low (below 10 wt%) and high (above 10 wt%) GO loading form Structures I and II, respectively. The formation of these unique structures is attributed to the GO dispersion effect and similar behaviour has been reported for GO and nanowires[37], or GO and polystyrene[38].

Structure I schematically represents the intercalation of NPs between the GO sheets, as seen in the HRTEM micrograph in Fig. 2f. In this case, the hydroxylated iron complexes are able to homogeneously anchor onto both the surfaces and edges of exfoliated GO sheets through the oxygenated functional groups, i.e. hydroxyl, epoxy and carboxyl. Further condensation of complexes leads to the formation of nuclei and growth of Fe_3O_4 crystallites onto GO sheets as a result of redox reaction. Likewise, this correlates well with the observed variation in the desorption branch of isotherms between relative pressures of 0.55–0.4 of the nanocomposites as compared to 0.75–0.4 of the Fe_3O_4 NPs as displayed in Fig. 1a. This effect may be associated with the resultant pore structure from the combination of different building blocks between the GO sheets and Fe_3O_4 NPs. This finding can be further corroborated with the featured pore width of ≤10 nm for the nanocomposites that was not observed in pure Fe_3O_4 NPs as presented in Fig. 1b.

Meanwhile, Structure II is correlated with deposition of Fe_3O_4 NPs mainly onto the exterior surface of GO stacking at higher GO loading. The anticipated GO stacking may be ascribed to the reduction in the degree of exfoliation as the concentration of GO increases. High GO loading may induce a dominant effect of GO stacking through the π-π interactions which correspond to the van der Waals and hydrophobic fields around the carbon basal plane of GO sheets. In fact, this proposed structures are in well agreement with the surface area and pore volume profiles which showed nearly 30% reduction in both once the GO loading increased to 15 wt% or more (Fig. 1c). Therefore, at higher GO loading, the aggregation of Fe_3O_4 NPs on the exterior surface of GO stacking might hinder the effective diffusion and contact between the reactants towards the active sites, which went against the ample formation of hydroxyl radicals to decompose AO7 during the reaction.

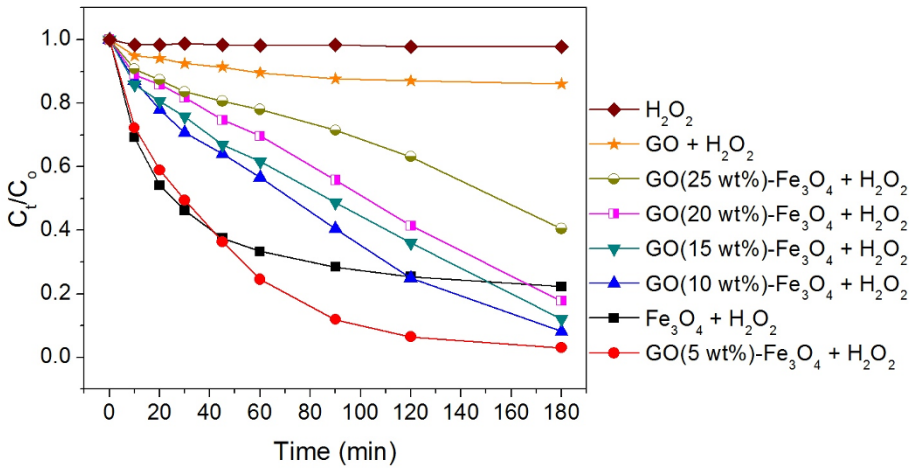

Figure 6 | Degradation profile of AO7 on GO, GO–Fe_3O_4 nanocomposites and Fe_3O_4 NPs samples in heterogeneous Fenton-like reaction. Experimental conditions: AO7 0.1 mM, H_2O_2 22 mM, catalyst 0.2 g L^{-1}, T = 25°C and pH 3.

Interestingly, the highest BET surface area of the nanocomposites was recorded at GO loading of 10 wt%, though the highest catalytic activity was found to be at GO loading of 5 wt% with the overall rate constant (k) of 0.02 min^{-1}. This indicates that the structure of the nanocomposites is not the only factor affecting their catalytic activity. With increasing GO loading, the catalytic activity of the nanocomposites gradually decreased, which means that there is a strong correlation between the catalytic activity and C–C/C–O ratio (Fig. 5). The higher reduction degree of GO at low GO loading promotes the transfer of electrons between Fe_3O_4 and GO through Fe-O-C bonds, which is beneficial for the degradation of AO7. The nanocomposite of 5 wt% GO loading delivered similar catalytic activity with the bare Fe_3O_4 NPs during the first 45 minutes of reaction as shown in Fig. 6, though the latter completely deactivated thereafter. Contrary to this detrimental result, the nanocomposite retained good stability by sustaining its activity throughout the entire reaction.

The degradation of AO7 occurs mainly at the solid-liquid interfaces of nanocomposites, where the formation of hydroxyl radicals ($HO^{\bullet}$) is due to the catalysed decomposition of hydrogen peroxide (H_2O_2) by the active sites ($\equiv Fe^{2+}/\equiv Fe^{3+}$) of Fe_3O_4 NPs. The symbol $\equiv$ represents the iron species bound to the surface of GO sheets. In addition, GO consists of unpaired π electrons by the presence of many semiconducting π-conjugated carbon sp^2 domain on its basal planes[39] which in turn are able to facilitate electron transfer between GO and iron centres[40]. This synergistic effect is beneficial in the regeneration of ferrous irons to speed up the redox cycle between the active sites, thus promoting the degradation and mineralisation of AO7.

The enhancement in chemical reactivity can be attributed to the synergistic effects between both optimized GO loading and Fe_3O_4 NPs. These effects may be explained by a combination of few factors. First, the high surface areas of exfoliated GO promotes good dispersion of Fe_3O_4 NPs onto GO sheets (Structure I). This was found to be beneficial in enhancing the mass transfer of reactants towards the active sites ($\equiv Fe^{2+}/\equiv Fe^{3+}$) during the reaction. Secondly, GO features a large aromatic ring structure on its basal plane that favours AO7 adsorption which has a similar aromatic ring structure through π-π interactions. This may provide an increase in AO7's local concentration[41] within the vicinity of the active sites to be further oxidised by the generated hydroxyl radicals[42]. Thirdly, the strong Fe_3O_4 NPs-GO interactions via Fe–O–C bonds facilitates the electron transfer between the NPs and the semiconducting GO sheets[40]. Lastly, the regeneration of ferrous ions was facilitated during the reaction possibly owing to the partial reduction in GO that helps electron transport to speed up the redox cycle between the active sites ($\equiv Fe^{2+}/\equiv Fe^{3+}$). This is evident for the low GO 5 wt% nanocomposite (see Fig. 5) as the C-C/C-O ratio is the highest thus demonstrating a higher removal of the oxygenated functional groups compared with the other nanocomposites at higher GO loading. In summary, this work demonstrates the structural and morphological relationship of GO–Fe_3O_4 nanocomposites at varies GO loadings on the overall catalytic activity of AO7 degradation in the heterogeneous Fenton-like oxidation.

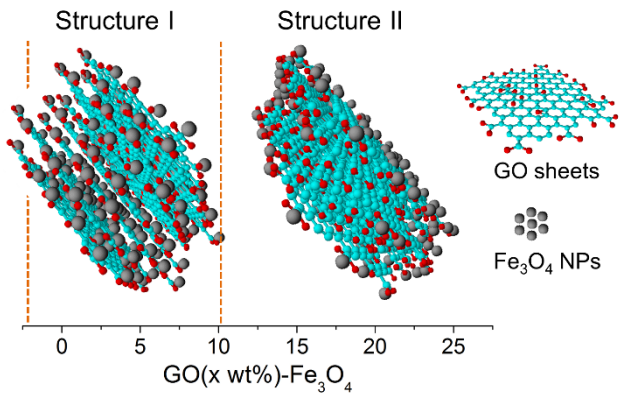

Figure 7 | The proposed two different structures of the GO–Fe_3O_4 nanocomposites at transitional GO loading of 10 wt% (the cyan, red and grey ball and stick model correspond to the carbon skeleton of GO sheet, oxygenated functional groups and Fe_3O_4 NPs, respectively).

Methods

Materials and preparation of GO–Fe_3O_4 nanocomposites. Graphite flakes, $FeCl_3{\cdot}6H_2O$ (97%), $FeCl_2{\cdot}4H_2O$ (99%) and AO7 (Orange II; 85%) were purchased from Sigma-Aldrich. All other reagents and solvents employed for synthesis were of analytical grade and used as received. Graphite oxide was synthesised via a modified Hummers method[43,44] and subsequently exfoliated by ultrasonication to attain an aqueous dispersion of GO. The GO–Fe_3O_4 nanocomposites were synthesised by co-precipitating pre-hydrolysed ferric and ferrous salts in the presence of GO. Briefly, an aqueous solution (100 mL) containing $FeCl_3{\cdot}6H_2O$ (4 mmol) and $FeCl_2{\cdot}4H_2O$ (2 mmol) was prepared with an initial pH of 1.48. However, GO sheets are prone to stack together at such low pH solutions, thus diminishing the effective surface of GO[45]. To address this problem, GO was not added into the mixture until the pH was adjusted to pH 4 via addition of NaOH (1 M). Subsequently, the GO solution (50 mL, 0.55 mg/mL) was gradually added into the pH 4 solution and stirred for another 30 min giving rise to a stable and homogeneous mixture. An appropriate amount of NaOH (1 M) was continuously added into this mixture to reach a pH of 10. The mixture was aged at constant stirring for a further 30 min at room temperature. The resulting black precipitate was magnetically separated and washed three times with deionized water and ethanol prior drying in an oven at 60°C for 48 h. The GO loadings for GO–Fe_3O_4 were set at 5, 10, 15, 20 and 25 wt%, respectively. Pure Fe_3O_4

NPs were also prepared via an analogous method without the addition of GO solution, for comparison purpose only.

Characterisation. Brunauer-Emmett-Teller (BET) specific surface area and pore volume were measured by nitrogen sorption using a Micromeritics Tristar 3020. The pore size distribution for each sample was calculated using non-local density functional theory (NLDFT), from the desorption branch of the isotherms. Microstructural investigation was carried out using a transmission electron microscopy (TEM, JOEL 1010) operated at 100 kV, and high-resolution transmission electron microscopy (HRTEM, JOEL 2010) with an acceleration voltage of 200 kV. Micrographic grids were prepared by placing a drop of diluted sample dispersion in ethanol onto a carbon-coated copper grid and dried at room temperature. X-ray photoelectron spectroscopy (XPS) was performed on Kratos Axis ULTRA X-ray photoelectron spectrometer equipped with monochromatic Al Kα ($h\nu = 1486.6$ eV) radiation to quantitatively analysed the chemical composition of samples. To determine the chemical functionality of the samples, the O 1 s and C 1 s spectra were curve fitted by combining the components and minimizing the total square-error fit of less than 2%. The curve fitting was performed using a Gaussian–Lorentzian peak shape and Shirley background function. The C 1 s photoelectron binding energy was set at 284.6 eV and used as reference for calibrating others peak positions.

Catalytic experiment. In order to investigate the catalytic activity of the as prepared GO–Fe_3O_4 nanocomposites, degradation of AO7 was studied in a heterogeneous Fenton-like reaction. All experiments were performed using GO–Fe_3O_4 (0.2 g L^{-1}) in AO7 (0.1 mM) aqueous solution of 250 mL at 25°C and pH 3. Prior to the batch runs, the initial pH of AO7 solution was adjusted with NaOH (1 M) or HCl (1 M) to 3. The reactions were initiated by adding H_2O_2 (22 mM) into the suspension and stirred at 350 rpm after 30 min of dark adsorption. Samples were periodically withdrawn, filtered through 0.2 μm Milipore syringe filters and immediately analysed. The AO7 degradation as a function of the time was analysed by measuring the absorbance of the solution at λ_{max} 484 nm using an UV-Vis spectrophotometer (Evolution 220, Thermo Fisher Sci.).

1. He, H. & Gao, C. Supraparamagnetic, conductive, and processable multifunctional graphene nanosheets coated with high-density Fe_3O_4 nanoparticles. *ACS Appl. Mater. Interfaces* **2**, 3201–3210 (2010).
2. Wei, Y. *et al*. Synthesis and cellular compatibility of biomineralized Fe_3O_4 nanoparticles in tumor cells targeting peptides. *Colloids Surf. B* **107**, 180–188 (2013).
3. Xu, L. & Wang, J. Fenton-like degradation of 2,4-dichlorophenol using Fe_3O_4 magnetic nanoparticles. *Appl. Catal. B* **123–124**, 117–126 (2012).
4. Thanikaivelan, P., Narayanan, N. T., Pradhan, B. K. & Ajayan, P. M. Collagen based magnetic nanocomposites for oil removal applications. *Sci. Rep.* **2**, 230; DOI:10.1038/srep00230 (2012).
5. Moodley, P., Scheijen, F. J. E., Niemantsverdriet, J. W. & Thüne, P. C. Iron oxide nanoparticles on flat oxidic surfaces—Introducing a new model catalyst for Fischer–Tropsch catalysis. *Catal. Today* **154**, 142–148 (2010).
6. Huazhang, L., Caibo, L., Xiaonian, L. & Yaqing, C. Effect of an iron oxide precursor on the H_2 desorption performance for an ammonia synthesis catalyst. *Ind. Eng. Chem. Res.* **42**, 1347–1349 (2003).
7. Bogdanov, S. S., Aleksić, B. D., Mitov, I. G., Klisurski, D. G. & Petranović, N. A. Comparative study of the reduction kinetics of magnetites and derived ammonia synthesis catalysts. *Thermochim. Acta* **173**, 71–79 (1990).
8. Zhang, S. *et al*. Superparamagnetic Fe_3O_4 nanoparticles as catalysts for the catalytic oxidation of phenolic and aniline compounds. *J. Hazard. Mater.* **167**, 560–566 (2009).
9. Zhu, M. & Diao, G. Synthesis of Porous Fe_3O_4 nanospheres and its ppplication for the catalytic degradation of xylenol orange. *J. Phys. Chem. C* **115**, 18923–18934 (2011).
10. Gao, L. *et al*. Intrinsic peroxidase-like activity of ferromagnetic nanoparticles. *Nat. Nanotechnol.* **2**, 577–583 (2007).
11. Gao, Y. *et al*. Fluorometric method for the determination of hydrogen peroxide and glucose with Fe_3O_4 as catalyst. *Talanta* **85**, 1075–1080 (2011).
12. Wei, H. & Wang, E. Fe_3O_4 magnetic nanoparticles as peroxidase mimetics and their ppplications in H_2O_2 and glucose detection. *Anal. Chem.* **80**, 2250–2254 (2008).
13. Deng, J., Wen, X. & Wang, Q. Solvothermal in situ synthesis of Fe_3O_4-multi-walled carbon nanotubes with enhanced heterogeneous Fenton-like activity. *Mater. Res. Bull.* **47**, 3369–3376 (2012).
14. Thi Dung, N., Ngoc Hoa, P., Manh Huy, D. & Kim Tham, N. Magnetic Fe_2MO_4 (M:Fe, Mn) activated carbons: Fabrication, characterization and heterogeneous Fenton oxidation of methyl orange. *J. Hazard. Mater.* **185**, 653–661 (2011).
15. Song, S., Rao, R., Yang, H., Liu, H. & Zhang, A. Facile synthesis of Fe_3O_4/MWCNTs by spontaneous redox and their catalytic performance. *Nanotechnol.* **21**, 185602–185607 (2010).
16. Prakash, A., Chandra, S. & Bahadur, D. Structural, magnetic, and textural properties of iron oxide-reduced graphene oxide hybrids and their use for the electrochemical detection of chromium. *Carbon* **50**, 4209–4219 (2012).
17. Fan, W. *et al*. Hybridization of graphene sheets and carbon-coated Fe_3O_4 nanoparticles as a synergistic adsorbent of organic dyes. *J. Mater. Chem.* **22**, 25108–25115 (2012).
18. Zeng, T., Zhang, X.-l., Ma, Y.-r., Niu, H.-y. & Cai, Y.-q. A novel Fe_3O_4-graphene-Au multifunctional nanocomposite: green synthesis and catalytic application. *J. Mater. Chem.* **22**, 18658–18663 (2012).
19. Choi, Y. *et al*. Hybrid gold nanoparticle-reduced graphene oxide nanosheets as active catalysts for highly efficient reduction of nitroarenes. *J. Mater. Chem.* **21**, 15431–15436 (2011).
20. Wu, H., Gao, G., Zhou, X., Zhang, Y. & Guo, S. Control on the formation of Fe_3O_4 nanoparticles on chemically reduced graphene oxide surfaces. *CrystEngComm* **14**, 499–504 (2012).
21. He, G. *et al*. Fe_3O_4@graphene oxide composite: A magnetically separable and efficient catalyst for the reduction of nitroarenes. *Mater. Res. Bull.* **48**, 1885–1890 (2013).
22. Song, Y., He, Z., Hou, H., Wang, X. & Wang, L. Architecture of Fe_3O_4–graphene oxide nanocomposite and its application as a platform for amino acid biosensing. *Electrochim. Acta* **71**, 58–65 (2012).
23. Dong, Y.-l. *et al*. Graphene oxide-Fe_3O_4 magnetic nanocomposites with peroxidase-like activity for colorimetric detection of glucose. *Nanoscale* **4**, 3969–3976 (2012).
24. Su, J., Cao, M., Ren, L. & Hu, C. Fe_3O_4–graphene nanocomposites with improved lithium storage and magnetism properties. *J. Phys. Chem. C* **115**, 14469–14477 (2011).
25. Zhou, G. *et al*. Graphene-wrapped Fe_3O_4 anode material with improved reversible capacity and cyclic stability for lithium ion batteries. *Chem. Mater.* **22**, 5306–5313 (2010).
26. Geng, Z. G. *et al*. Highly efficient dye adsorption and removal: a functional hybrid of reduced graphene oxide-Fe_3O_4 nanoparticles as an easily regenerative adsorbent. *J. Mater. Chem.* **22**, 3527–3535 (2012).
27. Chandra, V. *et al*. Water-dispersible magnetite-reduced graphene oxide composites for arsenic removal. *ACS Nano* **4**, 3979–3986 (2010).
28. Zhou, J., Song, H., Ma, L. & Chen, X. Magnetite/graphene nanosheet composites: interfacial interaction and its impact on the durable high-rate performance in lithium-ion batteries. *RSC Adv.* **1**, 782–791 (2011).
29. Adenier, A. *et al*. Covalent modification of iron surfaces by electrochemical reduction of aryldiazonium salts. *J. Am. Chem. Soc.* **123**, 4541–4549 (2001).
30. Shen, J. *et al*. One step synthesis of graphene oxide−magnetic nanoparticle composite. *J. Phys. Chem. C* **114**, 1498–1503 (2010).
31. Pei, S., Zhao, J., Du, J., Ren, W. & Cheng, H.-M. Direct reduction of graphene oxide films into highly conductive and flexible graphene films by hydrohalic acids. *Carbon* **48**, 4466–4474 (2010).
32. Zhou, G. *et al*. Oxygen bridges between NiO nanosheets and graphene for improvement of lithium storage. *ACS Nano* **6**, 3214–3223 (2012).
33. Combellas, C., Delamar, M., Kanoufi, F., Pinson, J. & Podvorica, F. I. Spontaneous grafting of iron surfaces by reduction of aryldiazonium salts in acidic or neutral aqueous solution. Application to the protection of iron against corrosion. *Chem. Mater.* **17**, 3968–3975 (2005).
34. Hurley, B. L. & McCreery, R. L. Covalent bonding of organic molecules to Cu and Al alloy 2024 T3 surfaces via diazonium ion reduction. *J. Electrochem. Soc.* **151**, B252–B259 (2004).
35. Fan, Z.-J. *et al*. Facile synthesis of graphene nanosheets via Fe reduction of exfoliated graphite oxide. *ACS Nano* **5**, 191–198 (2011).
36. Chen, W., Li, S., Chen, C. & Yan, L. Self-assembly and embedding of nanoparticles by in situ reduced graphene for preparation of a 3D graphene/nanoparticle aerogel. *Adv. Mater.* **23**, 5679–5683 (2011).
37. Li, Y. G. & Wu, Y. Y. Coassembly of graphene oxide and nanowires for large-area nanowire alignment. *J. Am. Chem. Soc.* **131**, 5851–5857 (2009).
38. Stankovich, S. *et al*. Graphene-based composite materials. *Nature* **442**, 282–286 (2006).
39. Matsumoto, Y. *et al*. Photoreaction of graphene oxide nanosheets in water. *J. Phys. Chem. C* **115**, 19280–19286 (2011).
40. Jasuja, K., Linn, J., Melton, S. & Berry, V. Microwave-reduced uncapped metal nanoparticles on graphene: Tuning catalytic, electrical, and raman properties. *J. Phys. Chem. Lett.* **1**, 1853–1860 (2010).
41. Qu, J.-C. *et al*. Facile synthesis of multifunctional graphene oxide/AgNPs-Fe_3O_4 nanocomposite: A highly integrated catalysts. *Chem. Eng. J.* **211–212**, 412–420 (2012).
42. Hu, X. *et al*. Adsorption and heterogeneous Fenton degradation of 17α-methyltestosterone on nano Fe_3O_4/MWCNTs in aqueous solution. *Appl. Catal. B* **107**, 274–283 (2011).
43. Hummers, W. S. & Offeman, R. E. Preparation of graphitic oxide. *J. Am. Chem. Soc.* **80**, 1339–1339 (1958).
44. Xiong, Z., Zhang, L. L. & Zhao, X. S. Visible-light-induced dye degradation over copper-modified reduced graphene oxide. *Chem. Eur. J.* **17**, 2428–2434 (2011).
45. Zubir, N. A., Zhang, X., Yacou, C. & Diniz da Costa, J. C. Fenton-like degradation of acid orange 7 using graphene oxide-iron oxide nanocomposite. *Sci. Adv. Mater.* **6**, 1–7 (2014).

Acknowledgments

The authors acknowledge funding support from The University of Queensland (NSRSF605709). The authors also acknowledge the facilities, and the scientific and technical assistance, of the Australian Microscopy & Microanalysis Research Facility at the

Centre for Microscopy and Microanalysis, The University of Queensland. Nor Aida Zubir gratefully acknowledges the generous financial support from Ministry of Higher Education Malaysia (MOHE) and Universiti Teknologi MARA (UiTM) for her PhD study leave. J.C. Diniz da Costa acknowledges support given by Australia Research Council Future Fellowship program (FT130100405).

Author contributions

N.A.Z. performed the experimental works, analysed results and wrote the manuscript. J.M. executed the HRTEM analysis. X.Z., C.Y. and J.C.D.d.C. advised N.A.Z. and reviewed the manuscript prior to submission.

Additional information

Competing financial interests: The authors declare no competing financial interests.

How to cite this article: Zubir, N.A., Yacou, C., Motuzas, J., Zhang, X.W. & Diniz da Costa, J.C. Structural and functional investigation of graphene oxide–Fe_3O_4 nanocomposites for the heterogeneous Fenton-like reaction. *Sci. Rep.* **4**, 4594; DOI:10.1038/srep04594 (2014).